

Glassy phase transition in immiscible steady-state two-phase flow in porous media

Santanu Sinha,¹ Humberto Carmona,² José S. Andrade Jr.,² and Alex Hansen¹

¹*PoreLab, Department of Physics, Norwegian University of Science and Technology, 7491 Trondheim, Norway.*

²*Departamento de Física, Universidade Federal do Ceará, Fortaleza, Brazil*

(Dated: March 10, 2026)

Two-phase flow in porous media is a ubiquitous phenomenon that has been studied for well over a century. However, we still lack a successful theory that predicts flow on a macroscopic length scale (the so-called *Darcy scale*) on the basis of a “microscopic” model. Here we show that the characteristic features of two-phase flow on the Darcy scale can be predicted by mapping the distribution of droplets in 2-phase flow onto the distribution of spins in a spin-glass model. The success of this approach is surprising, as two-phase flow is a non-equilibrium phenomenon, whereas the properties of the spin glass are obtained using equilibrium statistical mechanics. To obtain this mapping, we follow the approach of Meshulam and Bialek (Rev. Mod. Phys. **97**, 045002 (2025)) and use the Jaynes maximum entropy principle to derive the spin-glass Hamiltonian using machine learning trained on many realizations of the two-phase flow pattern in a dynamic pore network model. With this mapping, we can construct a “phase diagram” for the 2-phase flow system. We find that the critical line separating the paramagnetic phase from a spin glass phase coincides with the transition where the dependence of the rate of two-phase flow on the imposed pressure gradient changes from linear to non-linear. The glassy phase of the spin model coincides with a flow regime characterized by hysteresis and strong fluctuations over a wide range of time scales. It is tempting to identify this flow regime as a dynamic glass state.

Keywords: two-phase flow; porous media; spin-glass transition; Boltzmann machine learning

I. INTRODUCTION

In the 1980ies, there was a surge of interest in immiscible two-phase flow in porous media that coincided with the fractal revolution [1–3]. One of the most important results that came out of this period, was the phase diagram that Lenormand et al. [4] constructed for drainage processes. This is when a less wetting fluid with respect to the porous medium matrix invades a porous medium saturated by a more wetting fluid. The axes were the capillary number Ca , which is a non-dimensional measure of average flow velocity (definition in Equation (13)), and the viscosity ratio M between the invading and the defending fluids. The phase diagram revealed three types of injection patterns, capillary fingering when the capillary number is so low that capillary forces dominate, viscous fingers when the capillary number is large enough for the viscous and the capillary forces to compete while the viscosity of the defending fluid is larger than the invading fluid, and lastly stable displacement when the capillary number remains high, but the invading fluid viscosity is the larger.

Pretty as the fractals patterns are, they did not offer much insight into the large scale behavior of immiscible two-phase flow in porous media, which is the realm of practical applications such as in hydrology, soil science or reservoir engineering. The cause of this were the length scales involved. The fractal patterns of the eighties were pore-scale patterns whereas the practical applications occur on scales so large that the porous medium appears continuous. They have little to do with each other.

One may distinguish between four scales in porous media [5]: 1. the sub-pore scale, where the hydrodynamics and thermodynamics of confined spaces are relevant; 2. the pore scale, where e.g., the physics

of growth phenomena [6] are relevant; 3. the Darcy scale, where the porous medium appears continuous but structureless; and lastly, 4. the reservoir scale, where geological structure sets in.

Upscaling is to connect the descriptions of the problem on adjacent scales. Two upscaling problems stand out. The first one is connecting the description of immiscible two-phase flow at the pore scale to the Darcy scale. This boils down to constructing effective flow equations on the Darcy scale based on the physics at the pore scale. The second upscaling problem concerns how to deal with the disorder introduced by geological structure when moving from the Darcy scale to the reservoir scale. How does one deal with grid blocks that are in the hundreds of meters when there are geological structures influencing the flow on the scale of meters and up?

It is the first upscaling problem that will be relevant here. There are several approaches to this upscaling problem, getting from a pore scale description of the flow to a Darcy scale description, see Reference [7] for a review. It has become clear that the simplest flow state is steady-state flow. At the Darcy scale, this means that the variables describing the flow have well-defined stable time averages and that there are no gradients in the saturation field. Furthermore, the time averaged pressure gradient driving the flow is spatially uniform. In the laboratory, steady-state flow is created by simultaneously injecting the immiscible fluids into the sample. Away from the injection region and away from the edges of the sample, one finds steady-state flow.

The Payatakes group did extensive studies of steady-state flow at the pore scale in the nineties and the double naughts, see Avraam and Payatakes [8]. In this paper they classified the pore-scale description of steady-state flow into four regimes. At very high

Ca, they characterized the steady state as *drop traffic flow*. The less wetting fluid (from now on named the non-wetting fluid; the other fluid we refer to as the wetting fluid) forms sub-pore-scale droplets that move in the porous medium as traffic moves in a city. Hence, the name. At lower Ca, one encounters the *small ganglion regime*. Ganglions are fluid clusters that span across the pores. They are small in that the internal pressure drop across a given ganglion is too small to affect their motion. They are being carried along by the surrounding fluid. Moving further down in Ca, we enter the *large ganglion regime*. This when the ganglions are so large that their internal pressure drops enter an active role in how they move. Lastly, at low enough Ca, we find the *continuous path regime*. Now, the pressure gradients are so small that the ganglions do contribute to the flow, which is now carried by open pathways through the porous medium.

Berg et al. [7] have recently proposed a steady-state flow regime classification scheme at the Darcy scale. It is based on the constitutive relation between the average flow velocity and the average pressure gradient. In 2009, Tallakstad et al. [9, 10] observed in a two-dimensional model porous medium under steady-state flow conditions that the average flow velocity would depend on the average pressure gradient to an exponent,

$$v = -m|\nabla P|^\alpha, \quad (1)$$

where m is the mobility and $\alpha = 1.85 \pm 0.27$. This observation has been followed up in several papers by different groups, see e.g. [11–24]. Yiotis et al. [14] demonstrated that the power law constitutive equations appears in a window of capillary numbers Ca. Outside this window, i.e., at higher or lower Ca, the constitutive equation is linear. A pore-scale explanation for this behavior is that at low Ca, the capillary forces holding the fluid-fluid interfaces in place are too strong to be overcome, and the flow appears through open channels. Hence, the constitutive equation is linear. At higher capillary numbers, the pore-scale pressure gradients are large enough to mobilize the interfaces. This happens gradually as Ca is increased, resulting in the observed power law behavior. A quantitative explanation of this mechanism resulting in $\alpha = 2$ is given in [10]. When Ca is high enough, all interfaces that can be mobilized are moving, and the system reverts to linear behavior.

Berg et al. [7] refer to these three behaviors, linear–power law–linear, as regimes I, II and III. However, they go on to split regime I in two: Ia and Ib. Regime Ia is where the interfaces are frozen in place. However, as Ca increases, there are movement of the interfaces, resulting the ganglions changing shape. However, the transport of fluids through the system is still dominated by the open channels [26]. The time scales associated with these changes span widely [27]. Also Gao et al. [20] report a regime, which still being linear, fluctuates strongly. It is also a regime displaying strong hysteretic effects. This is regime Ib.

Thus we have three transitions: Ia–Ib, Ib–II and

II–III. The transition Ia–Ib we conjecture to be due to kinetic arrest [28], i.e., the time scales for interface motion exceed the time scale of the experiment as the Ca is lowered. It is, hence, not a transition in the sense that there are singularities present in the macroscopic variables. The same goes for the II–III transition. Roy et al. [29] have studied this transition computationally and analytically using a capillary fiber bundle model, finding its location depends on the system size. the larger the system, the more it moves towards the Ib–II transition. It is not a phase transition in the ordinary sense.

It is the nature of the Ib–II transition which is the focal point of this paper. We will demonstrate that it is a glassy transition, and as a consequence, *regime Ib is a glassy flow phase* [30].

We approach the nature of the Ib–II transition and the Ib regime by using the *Boltzmann machine learning method* [31]. Our model porous medium is a dynamical pore network model [32] which in this implementation consists of a bi-periodic diamond lattice where each link is a pore. Based on the saturation configurations in the network, we map the flow onto a spin model where the average saturation in each link and the saturation-saturation correlations between all pairs of links should be retained. We derive a configurational probability using the Jaynes maximum entropy principle, which resembles the probability distribution of a spin glass system. By training the spin model with the data from dynamical pore network simulations using Boltzmann Machine learning technique and measuring the higher order correlations, we show that the configurational probability reproduces the configurations obtained from the pore-network simulations. We then measure the magnetization, the magnetic susceptibility, the Edwards-Anderson order parameter and the spin glass susceptibility [30] for a wide range of flow parameters, and identified a spin glass critical line in the phase diagram for the spin model. When comparing it to the transition line between regimes Ib–II, we found that they match. Our conclusion is that regime Ib is a glassy flow regime and the transition to regime II, the power law regime, is a glass transition. As regime Ib shows both hysteretic behavior and fluctuations that span wide in time scale, this interpretation makes intuitive sense.

in Section II we derive the spin configurational probability based on measuring spatial correlations in the saturation distribution during steady-state two-phase flow in porous media. Section III describes the dynamic pore network model we use to generate the saturation distributions we measure. In the next Section IV we present the Boltzmann machine learning technique from which we determine the field constants and the coupling constants that define the spin model. In Section V we use this technique to investigate the character of the Ib–II transition and regime Ib. Section VI contains our summary and conclusions.

II. CONFIGURATIONAL PROBABILITIES

The aim of this section is to derive the configurational probability for spin configurations based on correlations in the saturation field during steady-state immiscible two-phase flow in porous media. The spin model consists of N interacting spins, $\sigma_i = \pm 1$. We use the Jaynes maximum entropy principle [33, 34] to derive the configurational probability $P(\{\sigma\})$, finding

$$P(\{\sigma\}) \propto \exp[-H(\{\sigma\})], \quad (2)$$

where

$$H(\{\sigma\}) = - \sum_i h_i \sigma_i - \sum_i \sum_{j < i} J_{ij} \sigma_i \sigma_j. \quad (3)$$

Here h_i are field couplings and J_{ij} are spin-spin couplings.

By running Monte Carlo simulations [57] of the spin model, it will reproduce the saturation correlations found in the flow model. An obvious question must be posed at this point: How can the equilibrium thermodynamics of the spin model mirror the dissipative dynamics of the dynamic pore network model? We point here to the mapping of the dissipative flow problem to an equilibrium statistical mechanics, and therefore also an equilibrium thermodynamics that has been proposed by Hansen et al. [35, 36] based on the idea that the fluid configurations in cuts orthogonal to the average flow direction behave as being in equilibrium since no configurational entropy in the sense of Shannon is produced in and between the cuts. The Jaynes generalized statistical mechanics based on Shannon entropy may then be invoked [33, 34].

We will here restrict ourselves to the (quasi-)two-dimensional (2D) porous media, though the whole approach is equally valid for three dimensions (3D). Common examples of such 2D systems used in the laboratory experiments are the Hele-Shaw cell filled with immovable glass beads [9], and etched PDMS or glass chips used in microfluidic experiments [37]. Snapshots of fluid configurations in such experiments can be recorded using high resolution cameras. The most detailed configuration in this case is governed by the resolution of the snapshots where each pixel can either be the solid of the porous medium, or one of the two fluids. The color of any pixel belonging to the pore space will vary from snapshot to snapshot depending on whether the pixel corresponds to the wetting or the non-wetting fluid. We may then define a fluid configuration similar to a magnetic spin system by considering a spin variable σ_i associated with a fluid pixel i , and the assigning a state $\sigma_i = \pm 1$ depending on the type of fluid in that pixel. The fraction of each type spins compared to the total number of spins will then be equal to the total saturation of the corresponding fluid in the system.

In case of computational experiments based on the lattice-Boltzmann method (LBM) [38] or dynamic pore network models [39], a configuration in the steady state can similarly be defined by associating

spin variables to the fluid voxels or pores respectively, and then by assigning their states based on the saturation of the fluids in the respective voxels or pores. This is a data driven approach, which requires large scale configurational data for a wide range of parameters. As already noted, we will in the following use a dynamic pore network (DPN) model, where the porous medium is modeled using a network of links and nodes [32]. This model is relatively less computationally expensive compared to the other methods such as LBM, and therefore is well suited for this study. We emphasize, however, that the whole approach can be implemented for other types of simulations, or experiments. Image analysis data from Hele-Shaw cell experiments [40] is a promising candidate for this approach we aim to use in future.

Let us now consider a pore network consisting of N pores. We associate a spin variable σ_i to each pore, where $i = 1, 2, \dots, N$. A link can contain bubbles of both the wetting and non-wetting fluids. We define the state of a spin by,

$$\sigma_i = \begin{cases} -1 & \text{if } s_i < \langle s \rangle \\ +1 & \text{if } s_i \geq \langle s \rangle \end{cases} \quad (4)$$

where s_i is the non-wetting saturation in the i th link, and $\langle s \rangle$ is the average pore-scale saturation of the non-wetting fluid. The set of the values of the spins, $\{\sigma_i \dots \sigma_N\}$, defines a configuration $\{\sigma\}$.

An important remark here is that by assigning spins to the links in this way, it may seem that we have by construction made the overall magnetization, defined as the average spin over all links, always equal to zero. This however is not so. Suppose we have a network with 100 links where 20 of them are fully filled with non-wetting liquid and the rest 80 are fully filled with the wetting liquid. We then have $\langle s \rangle = 0.2$, and therefore 80 of the links would be assigned spins pointing down and 20 would be assigned spins pointing up, making the overall magnetization non-zero.

We now aim to find a configurational probability $P(\{\sigma\})$ related to a spin configuration $\{\sigma\}$, such that two constraints, the average magnetization $\langle \sigma_i \rangle$ of each spin i , and the pairwise correlation $\langle \sigma_i \sigma_j \rangle$ between all spin pairs i and j , should be reproduced by the probability distribution. The average $\langle \dots \rangle$ here is over all the available configurations we can have from a simulation or experiment in the steady state. In terms of $P(\{\sigma\})$, these two constraints can be expressed as,

$$\begin{aligned} \langle \sigma_i \rangle &= \sum_{\{\sigma\}} \sigma_i P(\{\sigma\}) \quad \text{and} \\ \langle \sigma_i \sigma_j \rangle &= \sum_{\{\sigma\}} \sigma_i \sigma_j P(\{\sigma\}). \end{aligned} \quad (5)$$

We also have in addition the normalization criterion

$$\sum_{\{\sigma\}} P(\{\sigma\}) = 1. \quad (6)$$

With these constraints, the expression of $P(\{\sigma\})$ can be obtained by using the Jaynes maximum entropy

principle [33, 34] to maximize the Shannon information entropy defined as,

$$\Omega = - \sum_{\{\sigma\}} P(\{\sigma\}) \ln P(\{\sigma\}). \quad (7)$$

This can be done by using the Lagrange multiplier method and we outline it briefly in the following [31]. With Equations (5), (6) and (7) the Lagrangian can be constructed as,

$$\begin{aligned} \mathcal{L} = & - \sum_{\{\sigma\}} P(\{\sigma\}) \ln P(\{\sigma\}) + \theta \left[\sum_{\{\sigma\}} P(\{\sigma\}) - 1 \right] \\ & + \sum_i h_i \left[\sum_{\{\sigma\}} \sigma_i P(\{\sigma\}) - \langle \sigma_i \rangle \right] \\ & + \sum_i \sum_{j < i} J_{ij} \left[\sum_{\{\sigma\}} \sigma_i \sigma_j P(\{\sigma\}) - \langle \sigma_i \sigma_j \rangle \right], \end{aligned} \quad (8)$$

where θ , h_i and J_{ij} are the Lagrange multipliers. We then set $\partial \mathcal{L} / \partial P(\{\sigma\}) = 0$ to maximize \mathcal{L} resulting,

$$P(\{\sigma\}) = \frac{1}{Z} \exp \left[\sum_i h_i \sigma_i + \sum_i \sum_{j < i} J_{ij} \sigma_i \sigma_j \right], \quad (9)$$

where the normalization factor, or partition function is given by

$$\begin{aligned} Z &= \sum_{\{\sigma\}} P(\{\sigma\}) \\ &= \sum_{\{\sigma\}} \exp \left[\sum_i h_i \sigma_i + \sum_i \sum_{j < i} J_{ij} \sigma_i \sigma_j \right]. \end{aligned} \quad (10)$$

As we see, the configurational probability takes the form given in Equation (2), similar to a spin system with a Hamiltonian given by Equation (3). The parameters h_i and J_{ij} respectively play the role of the field constants and the coupling constants determining the different phases of the system, set by the quenched disorder of the sample. Averages over this disorder are needed to be taken into account in addition to the thermal averages. The number of the couplings grow with the system size making it challenging for the theory. Edward and Anderson provided the first model in 1975 for spin glass [41] which considers nearest neighbor interaction with J_{ij} s drawn from a binary or Gaussian distribution of random variables. Sherrington and Kirkpatrick (SK) introduced a solvable mean-field model [42] where all the spin pairs have direct interactions, which was later solved by Parisi [43]. For a Gaussian distribution of the couplings in the SK model, their solution reveals a phase space with three phases – ferromagnetic, paramagnetic and spin glass phases, defined by the standard deviation and mean of the distribution of the couplings [30].

Given this similar form of the configurational probability, we will explore how we can characterize such phases for steady-state two-phase flow, and how

the phases are related to different steady-state flow regimes. We will use the configurational data obtained from an interface tracking dynamic pore network model [32], which we describe briefly in the following.

III. DYNAMIC PORE NETWORK MODEL

In the pore network modeling of two-phase flow in porous media, the pore space of a porous matrix is represented by a network of links and nodes with idealized geometry, through which two immiscible fluids are transported [39]. Here we are using a *dynamic* pore network (DPN) that takes the effect of both viscous and capillary forces into account in moving the fluids. The fluid displacements are tracked by the position of all the fluid-fluid interfaces in the network. The pores consisting of a narrow pore throat between two wider pore bodies are modeled by hour-glass shaped composite links. All the pore space of the medium is therefore accounted for by the links, and the nodes of the network denote only the positions of the link intersections. While we are only considering 2D networks here, the model can be used for any network topology, also in 3D.

We consider a network of $L \times L = N$ links embedded in a 2D diamond lattice. This is illustrated in Figure 1 (a) for a network of $16 \times 16 = 256$ links. There are periodic boundary conditions in both directions as indicated by the blue and red nodes in the figure. This makes the system closed and the total volumetric saturation of the fluids therefore remain constant with time. All the links have the same length of $l = 1$ mm, whereas the average radius r_i of a link i is drawn from a uniform distribution of random numbers in the range between $0.1l$ to $0.4l$. This is indicated by the variation in the widths of links in the figure. We set the viscosity ratio $M = 1$. A typical distribution of two fluids inside the link is shown by the gray and blue colors indicating wetting and non-wetting bubbles. This model deals with system that do not have film flow or corner flow. For a fully developed laminar flow of incompressible fluids inside every link, the equation for the volumetric flow rate ϕ_i at any instance inside a link is given by [4, 44],

$$\phi_i = - \frac{\kappa_i}{l \mu_i} \left[\Delta p_i - \sum_k p'_i(\epsilon_k) \right], \quad (11)$$

where, Δp_i is the pressure drop between the two nodes across the link i . Here κ_i is the mobility of the link, and we consider a circular cross section for which $\kappa_i = \pi r_i^4 / 8$ for the Hagen–Poiseuille flow. The term μ_i is the effective viscosity of the fluids present inside that link at that instance. This is given by $\mu_i = s_i \mu_n + (1 - s_i) \mu_w$, where μ_w and μ_n are the viscosities of the wetting and non-wetting fluids respectively, and s_i is the volumetric saturation of the non-wetting fluid in that link, i.e., the proportion of the link volume that is occupied by the non-wetting fluid.

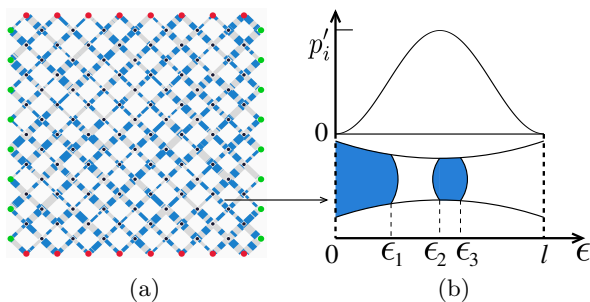


FIG. 1. (a) A pore network consisting 16×16 links on a 2D diamond lattice. The bonds in the lattice represent composite pores and the black dots represent the position of nodes. The thickness of the bonds indicates their average diameter. The gray and blue parts of the links indicate wetting and non-wetting bubbles. There is periodic boundary condition in both the horizontal and vertical directions, which is indicated by the green nodes on the vertical boundaries being identical nodes. The same is true for the red nodes on the horizontal boundaries. Shape of one composite link in terms of interfacial pressure (p'_i) is shown in (b) bottom where ϵ_1 , ϵ_2 and ϵ_3 show the position of three interfaces. The variation of p'_i at an interface along the length of the tube follows Equation (12), which is indicated in (b) top.

The second term with a summation inside the bracket in Equation (11) corresponds to the interfacial pressure (p'_i) associated with the fluid-fluid interfaces. For a hour-glass shaped composite link, this pressure will vary along the link and will be a function of the interface position. We model this functional form with a modified Young-Laplace equation [45–47] given by,

$$|p'_i(\epsilon)| = \frac{2\gamma}{r_i} \left[1 - \cos\left(\frac{2\pi\epsilon}{l}\right) \right], \quad (12)$$

where γ is the surface tension between the two fluids and ϵ is the position of the interface. This is illustrated in Figure 1 (b) which shows three interfaces at positions ϵ_1 , ϵ_2 and ϵ_3 . The summation in Equation (11) is over all the interfaces inside the link i where proper signs for p'_i need to be accounted depending on the direction of the capillary force.

Finally, we have from Kirchoff law $\sum_{i \in n_j} \phi_i = 0$ at every node for incompressible fluids. Here n_j is the number of links connected to a node j . This leads to a set of linear equations which we solve by conjugate gradient method [48] with necessary boundary conditions such as a global pressure drop or a total flow rate. The solutions provide local pressures at nodes, which are then used to calculate the link flow rates ϕ_i . All the interfaces are displaced in the direction of the flow in respective links with a small time step Δt . This changes the position of the interfaces and therefore the pressure distribution across the network. We solve for the pressures again and the process is repeated. This is how the fluids are transported and different fluid configurations are generated.

An important point in the context of the present study here is the time interval Δt . In this model Δt is chosen in such a way that the maximum displace-

ment of any interface should not exceed more than 10% of the respective link. This is done by calculating $\Delta t = 0.1l/v_{\max}$ at every time step, where v_{\max} is the fastest fluid velocity among all links. If there is a continuous flow channel across the network in the direction of global pressure drop, fluids in that channel should therefore need minimum $10L$ time steps to cross the whole network. As for this study we need the collection of configurations that are not correlated in time, we recorded configurations in steady state with an interval of every $2 \cdot 10L$ time steps.

A technical detail of the model is about how to distribute the fluids from links to neighboring links through the nodes. This is done by calculating the total volume of the wetting and non-wetting fluids (V_j^w and V_j^n respectively, and $V_j^w + V_j^n = V_j$) arriving at every node j from the connected links in which the flow is towards the node (incoming links). These volumes are then distributed as new bubbles in the connected links in which the flow is away from the node (outgoing links). The volume of these new wetting and non-wetting bubbles in an outgoing link i are given by $V_i^w = \phi_i \Delta t V_j^w / V_j$ and $V_i^n = \phi_i \Delta t V_j^n / V_j$ respectively. This implies that the ratio of the total new volumes ($V_i^w + V_i^n$) in between different outgoing links are the same as the ratio of the flow rates ϕ_i in those links, and the ratio between the V_i^w and V_i^n in any individual outgoing link is the same as the ratio between the total incoming wetting and non-wetting volumes at the corresponding node.

Simulations in this study are performed at constant capillary numbers Ca defined as,

$$Ca = \frac{Q\mu}{A\gamma}, \quad (13)$$

where Q is total flow rate of the fluids in the direction of global pressure drop ΔP . Here γ is the surface tension between the fluids, μ is the total effective viscosity, and A is the average cross-sectional area measured as $A = \sum_i \pi r_i^2 / L$. Here we considered $\gamma = 0.03$ N/m and equal viscosities for the two fluids with $\mu = 0.1$ Pa.s. We then varied Ca by changing the total flow rate Q .

The model has been tested against numerous experimental [16, 49] and theoretical [13, 50] results. It can simulate steady-state flow with different boundary conditions, as well as the drainage displacements to produce capillary and viscous fingers [51]. The model is also applicable to 3D porous networks reconstructed from real samples [16].

IV. BOLTZMANN MACHINE LEARNING

In this section we adapt the Inverse Ising modeling, also known as Boltzmann machine learning (BLM) method [31], to determine the distribution of the local field couplings h_i and coupling constants J_{ij} related to the underlying Hamiltonian given in Equation (3) from the DPN simulation. The method can be applied to a wide variety of problems ranging from biological

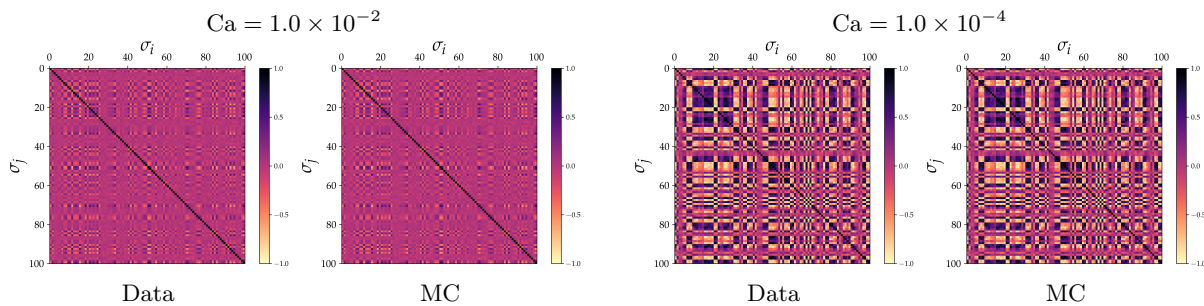


FIG. 2. Matrix plots of $\langle \sigma_i \sigma_j \rangle$ comparing the pore network simulation data and the MC sampling data after learning a specific network sample. The plots here are for $S_n = 0.3$, and we show two different Ca . For both, the maps from MC are visually indistinguishable from the data, indicating the convergence of the Boltzmann machine learning computations.

networks [52, 53] and trade networks [54] to bird flocking [55, 56], where the system can be mapped to an Ising-like model.

The idea is to obtain the values of h_i and J_{ij} for the probability distribution function $P(\{\sigma\})$, that best reproduce the configurations obtained from the simulation data. This is done by minimizing the difference between the target probability distribution P^{Data} related to the data (here the DPN simulations), and the probability distribution (P^{MC}) that follow function $P(\{\sigma\})$ given in Equation (9). To generate configurations with $P(\{\sigma\})$ we use Monte Carlo (MC) simulations [57]. The distance between two statistical distributions are measured using Kullback-Leibler (KL) distance (D_{KL}) given by,

$$D_{\text{KL}}(P^{\text{Data}} \parallel P^{\text{MC}}) = \sum_k P_k^{\text{Data}} \ln \left(\frac{P_k^{\text{Data}}}{P_k^{\text{MC}}} \right), \quad (14)$$

where the sum is over all possible configurations. To minimize D_{KL} with respect to h_i and J_{ij} , we use the iterative gradient descent method,

$$\begin{aligned} h_i(\tau + 1) &= h_i(\tau) - \eta \left. \frac{\partial D_{\text{KL}}}{\partial h_i} \right|_{\tau} \quad \text{and} \\ J_{ij}(\tau + 1) &= J_{ij}(\tau) - \eta \left. \frac{\partial D_{\text{KL}}}{\partial J_{ij}} \right|_{\tau}, \end{aligned} \quad (15)$$

where τ is the iteration step, and η is the learning rate. By using derivatives of D_{KL} , and the definition of $P^{\text{MC}} \equiv P(\{\sigma\})$ given in Equation (5), we have from Equations (14) and (15) that

$$\begin{aligned} J_{ij}(\tau + 1) &= J_{ij}(\tau) + \eta [\langle \sigma_i \sigma_j \rangle^{\text{Data}} - \langle \sigma_i \sigma_j \rangle_{\tau}^{\text{MC}}] \quad \text{and} \\ h_i(\tau + 1) &= h_i(\tau) + \eta [\langle \sigma_i \rangle^{\text{Data}} - \langle \sigma_i \rangle_{\tau}^{\text{MC}}], \end{aligned} \quad (16)$$

where the quantities $\langle \dots \rangle^{\text{Data}}$ are measured from the DPN simulation data at the beginning of BML iterations, and $\langle \dots \rangle^{\text{MC}}$ are measured from the MC simulations at every iteration τ .

The learning rate η determines the rate of update during the gradient descent method, which is a crucial parameter for the optimal performance of the algorithm. This affects the speed and stability of the convergence. A too high or too low learning rate can result in overshoot or very slow convergence, making the simulations impossible to reach solutions with

good accuracy. A general practice is to start with a relatively large value of η , and then reduce it gradually using a learning rate scheduler. There are different types of schedulers which work best for different types of problems. By trying a few different schedulers, we found that the scheduler *ReduceLROn-Plateau* [58] works best for this study. This method monitors the loss (E) during the iteration, and reduces η by a factor when E stops improving for a specific number of iterations. Here the loss is defined as,

$$\begin{aligned} E &= \frac{1}{N} \sum_i (\langle \sigma_i \rangle^{\text{Data}} - \langle \sigma_i \rangle_{\tau}^{\text{MC}})^2 \\ &+ \frac{1}{N(N-1)} \sum_i \sum_{j < i} (\langle \sigma_i \sigma_j \rangle^{\text{Data}} - \langle \sigma_i \sigma_j \rangle_{\tau}^{\text{MC}})^2, \end{aligned} \quad (17)$$

which calculates the mean squared difference of correlations and averages between the data and MC.

We performed BML computations using data sets obtained from DPN simulations for different values of S_n and Ca . The values of $\langle \sigma_i \rangle^{\text{MC}}$ and $\langle \sigma_i \sigma_j \rangle^{\text{MC}}$ are calculated with Metropolis Monte Carlo simulation with the probability distribution function given in Equation (9). This requires measuring of $N(N-1)/2$ values for the correlations for each MC sample at every BML step which is computationally expensive. Our DPN simulations were performed with a 40×40 network which would lead to 1279200 values of couplings. Furthermore, a large number of MC samplings is necessary in the spin glass phase, as the configurations can stuck in a local minima for a long time. We also have a large parameter space (the complete detail of the parameter sets and the size of the data sets are provided in the next section). To reduce the computational time that is feasible to available resources, we coarse grained the system to a 10×10 network for the BML computations. This leads to $N = 100$ spins and 4950 values of couplings. We considered 2×10^5 MC sweeps for MC thermalization and 10^5 MC configurations for averaging in each BML iteration. We performed a minimum of 10^4 BML iterations for each case and then terminated the iterations when the loss E in Equation (17) reached a small enough value. The final values of h_i and J_{ij} are then considered at the end of the BML iterations.

To verify how the Hamiltonian in Equation (3) and

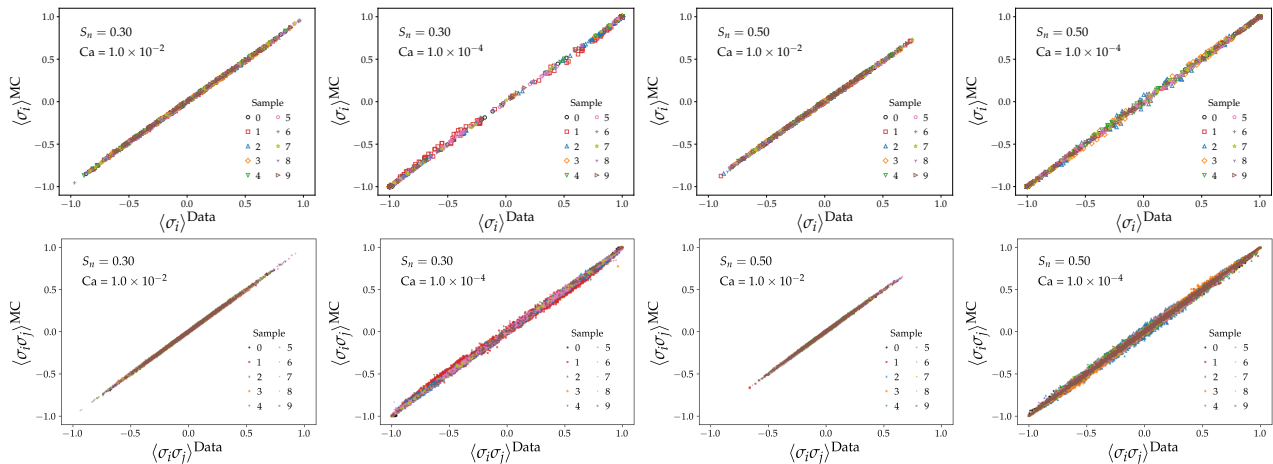


FIG. 3. Plots of $\langle \sigma_i \rangle^{\text{Data}}$ vs $\langle \sigma_i \rangle^{\text{MC}}$ (top row), and $\langle \sigma_i \sigma_j \rangle^{\text{Data}}$ vs $\langle \sigma_i \sigma_j \rangle^{\text{MC}}$ (bottom row), showing the comparison between DPN simulation data and BML computations. We show data for two saturations $S_n = 0.3$ and 0.5 , with two capillary numbers, $Ca = 1.0 \times 10^{-2}$ and 1.0×10^{-4} for each S_n . Each plot contains results for 10 different network samples.

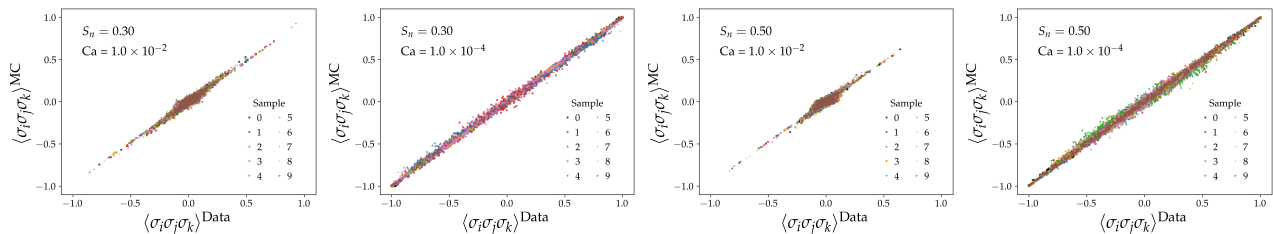


FIG. 4. Plots of 3-point correlations $\langle \sigma_i \sigma_j \sigma_k \rangle$ compared between the DPN data and MC samples. We show results for two saturations $S_n = 0.3$ and 0.5 , and two capillary numbers $Ca = 1.0 \times 10^{-2}$ and 1.0×10^{-4} for each S_n . Each plot contains results for 10 different network samples, and we plotted data only for 1000 randomly chosen unique triples $\{ijk\}$ for each sample.

the corresponding configurational probability $P(\{\sigma\})$ in Equation (9) reproduces two-phase flow data obtained from the DPN model, we show in Figure 2 the matrix plots of $\langle \sigma_i \sigma_j \rangle$ for two cases, which provides a visual comparison between the DPN data and the BML computations. We show for two values of Ca , and for both cases the plots from BML are visually indistinguishable from the DPN data. We see differences in the correlations between low and high capillary numbers. At high Ca , the correlations indicate a continuous variation around zero, whereas at the low Ca we see clustering of high positive or negative values. This indicates that the flow in different pores are highly correlated or anti-correlated at low Ca .

A more quantitative comparison between the DPN data and BML results are provided in Figure 3, where we plotted $\langle \sigma_i \rangle$ and $\langle \sigma_i \sigma_j \rangle$ between data and MC for all the values of i and j . We show results for two different saturations $S_n = 0.3$ and 0.5 with two Ca values for each case. Each plot contains data points for 10 network samples. We see that the data points follow the diagonal line with minimal deviations. This indicates that configurational probability $P(\{\sigma\})$ Equation (9) agrees well with DPN data.

The probability distribution $P(\{\sigma\})$ in Equation (9) was obtained with the constraints up to two point

correlations. In order to therefore verify whether the model can predict higher order correlations, we plotted in Figure 4 the three point correlations $\langle \sigma_i \sigma_j \sigma_k \rangle$ obtained from the DPN data and from MC, and the plots show that the model demonstrate the data with minimum deviations.

The values of local fields h_i and the coupling constants J_{ij} obtained from the BML computations with the DPN data are plotted in Figures 5 and 6. Each plot contains data from 10 different network samples. The histograms of h_i indicate that the values are mostly spread around zero, though at low Ca there are a few spins with very high positive or negative values of h_i . Such spins do not appear at high Ca , however the spread of h_i widens.

The distributions $p(J_{ij})$ shown in Figure 6 reveal a nontrivial form. The distributions for all the sets show the coupling constants are spread around zero with both positive and negative values, indicating a spin glass type system. However at low Ca , the $p(J_{ij})$ shows bimodal type distributions with two peaks for most of the samples, indicating there are two sets of correlated and anti-correlated pores. While increasing Ca , peaks at $J_{ij} = 0$ start appearing, and at high Ca all the distributions lead to a unimodal distribution.

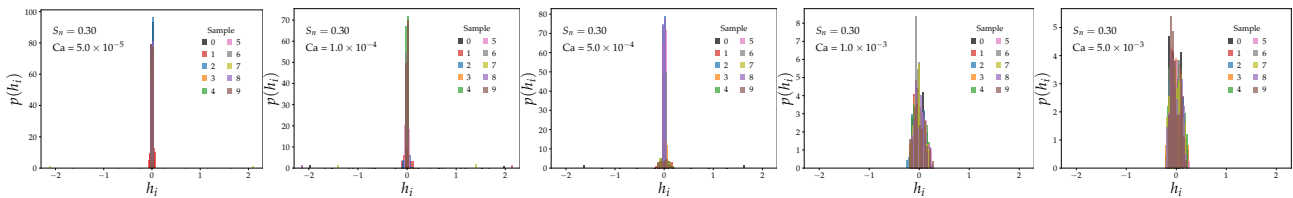


FIG. 5. Histograms of local field constants h_i for $S_n = 0.3$ at different capillary numbers. Each plot shows data for 10 different network samples.

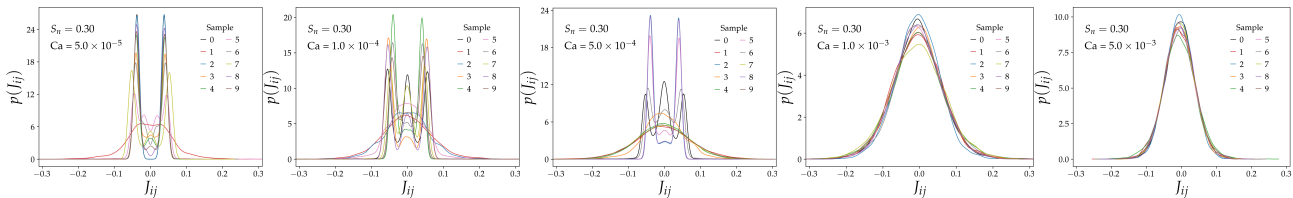


FIG. 6. Plots of the distributions of the coupling constant J_{ij} for $S_n = 0.30$. Here we show results for 5 capillary numbers. Each plot contains results for 10 different network samples. Apparently, all the distributions have a mean around zero, however at low Ca most samples show multiple peaks, indicating groups of highly correlated or anti-correlated couplings. There is also dominant sample-to-sample variations at low Ca. At high Ca, the coupling constants are spread around zero with a Gaussian-like distribution for all the samples.

V. THE GLASS TRANSITION AND GLASSY FLOW STATE

The paramagnetic (P) and ferromagnetic (F) phases in a spin system are characterized by zero and non-zero values of the total average magnetization (m) respectively, implying that the spin alignments to be random or in a specific direction. The characterization of a spin glass (SG) phase on the other hand is more subtle. There is no global alignment of spins in a specific direction similar to a paramagnetic phase, but the spins are now locally oriented. This is caused by the presence of both ferromagnetic ($J_{ij} > 0$) and antiferromagnetic ($J_{ij} < 0$) couplings (though it is not a sufficient condition) in the system, resulting in an inability to satisfy the coupling conditions for every spin pairs. This leads to *frustration* and rugged energy landscapes [30], with the appearance of disorderly frozen spin patterns making the spins locally magnetized.

By using data obtained from DPN simulations, we illustrate in Figure 7 that the spin model is in a spin glass phase at low capillary number ($Ca = 0.0005$), whereas such a phase is not present at high capillary number ($Ca = 0.2$). The global saturation of the non-wetting fluid is $S_n = 0.3$ here. The figure shows (i) the bubble distributions, (ii) the respective spin mappings using Equation (4), and (iii) $\langle \sigma_i \rangle^2$, indicating the degree of local magnetization. The applied global pressure drop is in the vertical directions in these figures. The spin representations for these two low and high capillary numbers show somewhat similar random spin orientations giving low values of m . However the degree of local magnetization $\langle \sigma_i \rangle^2$ is significantly different. At high Ca, $\langle \sigma_i \rangle^2$ shows uniformly zero values across the system for majority of spins, whereas at low Ca the majority of the spins

have very high degrees of local magnetization. Furthermore, patches of small value of $\langle \sigma_i \rangle^2$ can be observed at low Ca (b), which indicates the dominance of frozen pathway flow. These maps therefore seem to capture the different pore-scale flow patterns similar to what was described by Avraam and Payatakes [8]. We will discuss this further later on.

Two main observables to characterize these phases are total ferromagnetic magnetization m , and the Edwards-Anderson order parameter q . These are two order parameters which characterize the transitions between paramagnetic and ferromagnetic phases, and between paramagnetic and spin glass phases respectively. The spin glass order parameter q represents the degree of local magnetization. They are respectively,

$$m = \frac{1}{N} \left[\sum_i \langle \sigma_i \rangle \right]_a \quad \text{and} \quad q = \frac{1}{N} \left[\sum_i \langle \sigma_i \rangle^2 \right]_a, \quad (18)$$

where the sum is over all the N spins. The average $\langle \dots \rangle$ represents the average over different configurations for a specific sample, whereas $[\dots]_a$ represents the average over different network samples. The paramagnetic phase is characterized by $m = 0$ and $q = 0$, the ferromagnetic phase is characterized by $m \neq 0$ and $q > 0$, and the spin glass phase is characterized by $m = 0$ and $q > 0$. The other two relevant observables are the uniform susceptibility (χ_m) and spin glass susceptibility (χ_{sg}), which are defined as [59],

$$\chi_m = \frac{1}{NT} [\langle M^2 \rangle - \langle M \rangle^2]_a \quad \text{and} \quad \chi_{sg} = \frac{1}{NT^2} \left[\sum_{\langle i,j \rangle} (\langle \sigma_i \sigma_j \rangle - \langle \sigma_i \rangle \langle \sigma_j \rangle)^2 \right]_a, \quad (19)$$

where $M = \sum_i \sigma_i$. The uniform susceptibility χ_m diverges at the boundary between the P and F phases

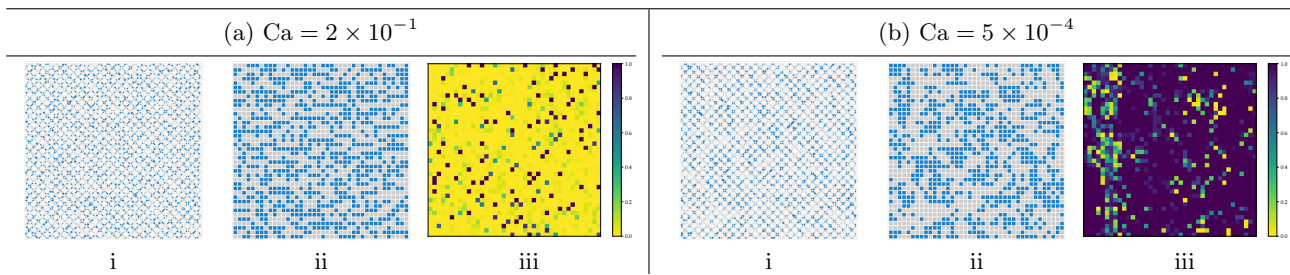


FIG. 7. Snapshots from dynamic pore network simulations illustrating the differences between steady-state flow states in the dynamic pore network model that give rise to paramagnetic and spin glass phases in spin model. The simulations were performed with a network of $40 \times 40 = 1600$ links, and a global non-wetting saturation of $S_n = 0.3$. We show two cases corresponding to the capillary numbers (a) $Ca = 2 \times 10^{-1}$ and (b) $Ca = 5 \times 10^{-4}$ for the same network. There are 3 figures for each case. Snapshots in (i) show the positions of wetting (gray) and non-wetting (blue) fluids in the network at a certain time step in steady state. The corresponding spin configurations, obtained using Equation (4) are shown in (ii) where the blue and gray dots represent $\sigma_i = +1$ and -1 respectively. The average $\sum_i \sigma_i / N$ over different time steps in the steady state returns low values of magnetization for both capillary numbers, $m \approx 0.026$ and ≈ 0.057 for (a) and (b) respectively. However, a noticeable difference is observed in the snapshots in (iii) which show $\langle \sigma_i \rangle^2$, highlighting local frozen spins at the low capillary number. This leads to a high value of the Edwards-Anderson order parameter $q \approx 0.884$ for (b), whereas a low $q \approx 0.088$ for (a).

whereas the spin glass susceptibility χ_{sg} diverges at the boundary between the P and SG phases.

To measure these observables we performed dynamic pore network simulations with constant capillary number (Ca) using networks containing $40 \times 40 = 1600$ links. Simulations were performed for 17 values of total non-wetting saturations from $S_n = 0.1$ to 0.9 with interval of 0.05 . For each saturation, we performed simulations with 53 different values of Ca in the range of 5×10^{-5} to 2×10^{-1} . This leads to a total of 901 independent simulation parameters. For each parameter set, we considered 100 different samples (realizations) of the network corresponding to the average $[\dots]_a$ in the Equations (18) and (19). For each sample, 1000 different fluid configurations were considered in steady state (the average $\langle \dots \rangle$). This leads to a total of 10^5 steady-state configurations for each parameter set. To reach the steady state, we typically skipped 10 pore-volumes of flow, which we found sufficient for a random initial distribution of the two fluids. In the steady state, we only measured at time intervals sufficient to avoid correlations between them (see Section III).

The steady-state fluid configurations were mapped onto spin configurations, from which we measure the observables defined in Equations (18) and (19). We show the results in Figure 8 for $S_n = 0.3$, where we plot m , q , χ_m and χ_{sg} as a function of the average steady-state pressure drop ΔP . We see that the magnetization m remains essentially unchanged at a low value, whereas the spin glass order parameter q rises sharply while decreasing the pressure drop. This indicates high degree of local magnetization at low Ca , while the total magnetization remains unchanged at a low value. We also see in Figure 8 (b), where the spin glass susceptibility χ_{sg} has a peak at a pressure value $\Delta P(\chi_{sg}^{\max})$ similar to where the sharp increase in q is observed. The uniform susceptibility χ_m do not show such a peak. These observations are exactly

those that signal a critical point separating a spin glass phase from a paramagnetic phase. These results show that the dynamic pore network model experiences a critical transition to a glassy state when Ca is lowered through the critical value.

A natural question here is therefore whether this transition from the paramagnetic to the glassy phase in the spin model, which is entirely characterized by the pore-scale fluid configurations, is related to any transition or crossover observed at the Darcy scale. As described briefly in the Introduction, Berg et al. [7] based their classification of Darcy scale phases on the constitutive relation relating flow velocity to pressure gradient. In the laboratory, velocities and pressure gradients are not observed directly. Rather, one observes the volumetric flow rate Q as a function of the pressure drop ΔP across the porous medium sample under steady-state conditions. Experiments and computations have established that while increasing the Ca from a low value, the relationship between Q and ΔP changes from a linear (regime I) to a non-linear power-law relationship, $Q \sim \Delta P^\alpha$, with $\alpha > 1$ (regime II) [11–25]. Certain systems have also shown the existence of a threshold pressure P_t in this regime, such that $Q \sim (\Delta P - P_t)^\alpha$ [13]. The origin of P_t is the absence of continuous pathways [46], creating a net pressure drop for the medium which the viscous pressure drop must overcome to start the flow. We note that $P_t \rightarrow 0$ as the system size increases [5, 29]. While increasing Ca further, the power law regime crosses over to another linear regime (regime III) displaying again a linear relationship between Q and $\Delta P - P_t$. The origin of these three regimes may be found in the dynamics of the fluid-fluid interfaces as described in the Introduction. However, the behavior is generic for bi-viscous fluids [60, 61].

Berg et al. [7] split regime I into a regime Ia, where the fluid-fluid interfaces are frozen and a regime Ib where the interfaces move, but there is no transport

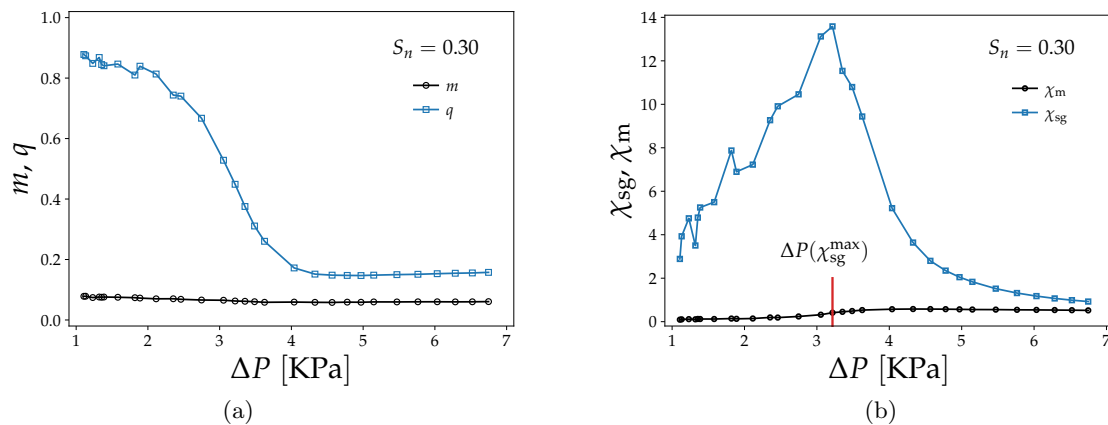


FIG. 8. Plots of (a) ferromagnetic and spin glass order parameters m and q , and (b) the uniform and spin glass susceptibilities χ_m and χ_{sg} in the spin model as a function of average steady state pressure drop ΔP for global non-wetting saturation $S_n = 0.3$ in the pore network model. The magnetization m remains low for the whole range of ΔP whereas q rises sharply with the decrease of ΔP , indicating a spin glass transition. This is supported by the plots in (b), where χ_{sg} shows a distinct peak at the pressure drop $\Delta P(\chi_{sg}^{\max})$, which is where q rises. The uniform susceptibility χ_m on the other hand remains low for the whole range of ΔP .

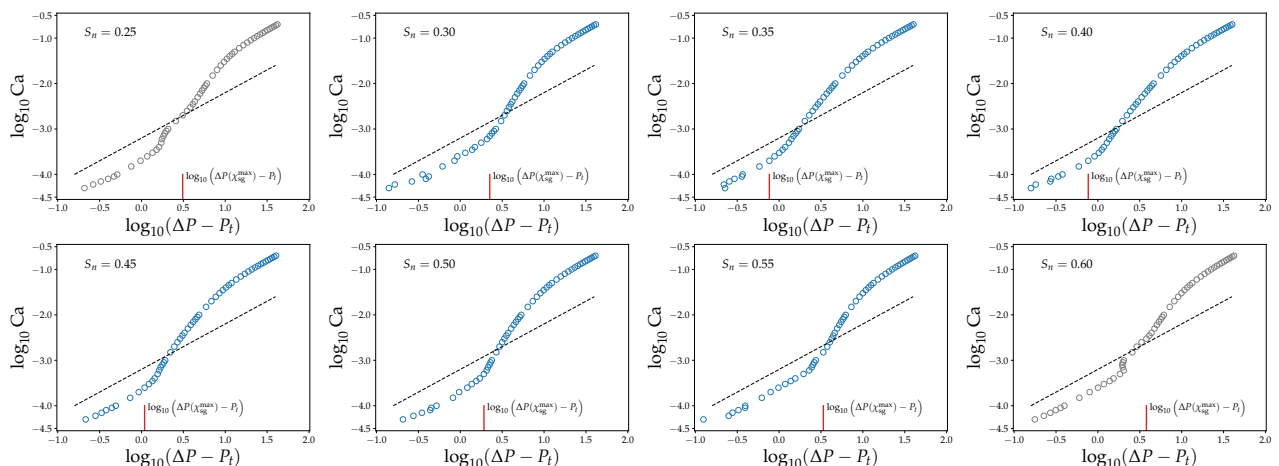


FIG. 9. Plots of $\log_{10} Ca$ as a function of $\log(\Delta P - P_t)$ in the steady state for different non-wetting saturations (S_n). The black dashed lines are drawn with slope 1, indicating a linear relationship between the steady state flow rate Q and the pressure drop ΔP . The data show that there are three regimes, two linear regimes at low and high Ca values, and a non-linear regime in between, named regimes I, II and III by Berg et al. [7]. The small vertical red lines indicate the positions of pressure drops $\Delta P(\chi_{sg}^{\max})$, where the spin glass susceptibilities χ_{sg} have the peak for respective saturations (see Figure 8 (b)). We find that these positions are comparable with the positions of the crossovers from the lower linear to the intermediate non-linear regime for intermediate saturations in the range $S_n = 0.30$ to 0.55 . This range is indicated with blue color plots. Outside this saturation range, these two positions do not match. In addition, the data also start to deviate from the three well-defined regimes outside this saturation range.

associated with this movement [26]. Gao et al. [20] investigated the transition from regime Ib to regime II, demonstrating that the onset of the non-linearity is characterized by large pressure fluctuations. This indicates that the onset of power law behavior is triggered by the merging and splitting of ganglions, termed as the intermittent flow [62], or by gradually mobilizing stranded ganglia population [63]. By comparing mechanical energy related to the viscous pressure drop to the surface energy needed to create fluid menisci, Zhang et al. [21] demonstrated that the onset of intermittency indeed matches with the transition from regime Ib to II.

As stated in the Introduction, the transition from regime II to III, is not a phase transition. Roy et al.

[29] demonstrated that the transition moves towards lower Ca when the system size is increased. The transition from regime Ia to Ib is also not a phase transition. Rather, it has all the hallmarks of a kinetic arrest transition where the time scales associated with the dynamics of phase Ib becomes longer than that of the experimental situation.

In order to identify the connection between the Darcy scale flow regimes with the glass transition that we observed here for the pore network flow, we measured average steady-state pressure drops ΔP for all the simulations. The simulations were performed for constant capillary numbers Ca , which set the total flow rate Q (Equation (13)). We show these results in Figure 9, where we plot $\log_{10} Ca$ as a function of

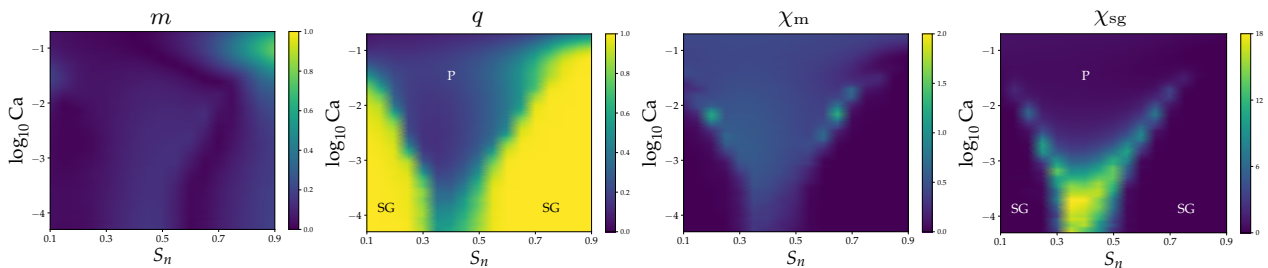


FIG. 10. Color maps showing the values of m , q , χ_m and χ_{sg} plotted against $(S_n, \log_{10} Ca)$. Each plot contains 901 data points. The maps for q and χ_{sg} show the P and SG phases distinctly indicating the phase boundaries between these phases. We observe that the Ca for transition from P to SG phase decreases as S_n approaches ≈ 0.4 . The maps for m and χ_m show some color gradient, however they are relatively very weak compared to q and χ_{sg} , and do not indicate any transition between P and F phases.

$\log_{10}(\Delta P - P_t)$ for different values of non-wetting saturation S_n . We see that for an intermediate range of saturations $S_n = 0.30$ to 0.55 , the plots show three distinct regimes, I, II and III, showing a non-linear regime in between two linear regimes. The dashed line is drawn with a slope of 1, indicating a linear relationship between Q and ΔP . The threshold pressure P_t are measured by fitting the data points of regime I to a straight line. We then added the small vertical red lines in the plots showing the values of $\Delta P(\chi_{sg}^{\max})$ for each S_n , which indicate the transition points to the glassy phase. The values of $\Delta P(\chi_{sg}^{\max})$ are obtained from the peaks of the spin glass susceptibilities χ_{sg} measured for different S_n , as indicated in Figure 8 (b). Surprisingly, the positions related to the glass transition fall at the values of ΔP where the crossover from regime I to regime II is observed. This explains the hysteretic behavior, the large fluctuations and the wide range of timescales seen in the intermittent regime: The transition Ib to II is a critical glass transition.

Here we mention that outside the intermediate range of $S_n = 0.30$ to 0.55 , our DPN data do not reproduce the transition between the regimes I and II well, as shown by the black plots in 9 for $S_n = 0.25$ and 0.60 . Consequently, we cannot find an agreement between the glassy transition point and crossover points between regime I and II outside this range of S_n . We therefore did not show the results for the extreme values of S_n . This may be due to the limitation of the DPN model at low capillary numbers.

The complete phase diagram on the Ca vs S_n space for all the 901 parameters is shown in Figure 10. The color maps for q and χ_{sg} show distinct separation between regions indicating the boundaries between the SG and P phases. The respective phases are marked on these plots. The plots for m and χ_m on the other hand do not show any significant separation, therefore the presence of an F phase is not observed on this space.

An observation from Figure 10 is that the value of Ca necessary for the transition to a glassy phase for any specific S_n decreases as S_n approaches to ≈ 0.4 from both sides. This value of S_n falls around the same value where S_n crosses the $F_n = S_n$ line, as

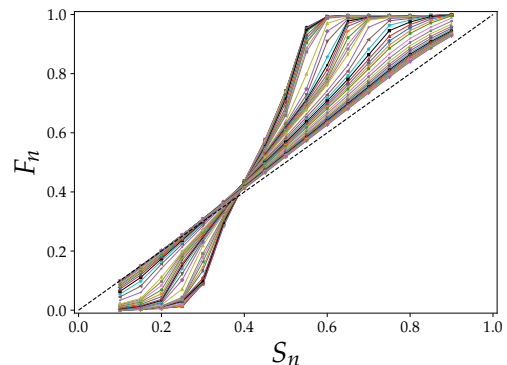


FIG. 11. Plot of non-wetting fractional flow (F_n) versus global non-wetting saturation (S_n) for 53 values of capillary numbers (Ca). The diagonal dashed line indicates the $F_n = S_n$, along which both the fluids will move with the same velocity. The individual curves correspond to different values Ca, the closest to the diagonal being the highest Ca while the farthest with the most step-like form being the lowest Ca.

shown in Figure 11. Here F_n is the non-wetting fractional flow in the steady state defined as $F_n = Q_n/Q$, where Q_n is the volumetric non-wetting flow rate. Different curves in Figure 11 correspond to different values Ca, where the curves approaching towards the dashed $F_n = S_n$ line correspond to the increase in Ca. Along the $F_n = S_n$ line, both the fluids flow with same velocity, similar to two miscible fluids as if there were no surface tension between the two fluids. We see in this figure that all the curves cross this line at around $S_n \approx 0.4$ for our DPN model. It therefore appears that as S_n approaches this value, the capillary forces become less effective to hold any fluid ganglion in place, thus pushing the glass transition towards lower Ca numbers.

VI. SUMMARY AND DISCUSSION

The aim of this work has been to find a description for the pore-scale configurational probability for immiscible two-phase flow in porous media, and then to establish a phase diagram for the steady state based on the configurations. We approached this by map-

ping the saturation patterns of two-phase flow in a dynamic pore network model onto a spin model such that it should retain the average saturation and the saturation-saturation correlations. A probability distribution function for such a spin system is obtained by using Jaynes maximum entropy principle. Then by training the spin model using Boltzmann machine learning method and measuring up to the three point correlation function, we show that the spin model reproduces the fluid configurations of the pore network model. We then analyzed the ensuing thermodynamic variables for a large number of flow parameters and build up a phase diagram. We display the resulting phase diagram in Figure 10. The axes of the plots are the non-wetting saturation S_n and the capillary number $\log_{10} \text{Ca}$. The third variable, the viscosity ratio, M is set to unity. The plots are thus cuts through a three-dimensional phase diagram. We see little structure with respect to the magnetization order parameter m and susceptibility χ_m . However, the Edwards-Anderson order parameter q and the spin-glass susceptibility χ_{sg} light up, signaling the presence of a spin-glass phase and a paramagnetic phase, with critical lines separating them.

Berg et al. [7] proposed a Darcy scale phase diagram based on the constitutive equation relating average flow velocity v to the average pressure gradient $|\nabla P|$. In terms of increasing capillary number Ca , the constitutive equation is linear (phase I), then it shifts to being a power law, see Equation (1) (phase II), and then it shifts back to being linear (III). Furthermore, phase I is split into a frozen phase Ia and a dynamic phase Ib [26]. The transition between phases Ia and Ib is a kinetic arrest, and therefore not a proper transition. The transition between phases II and III is also not a proper transition, but rather a saturation phenomenon: all fluid-fluid interfaces that can move, are moving in phase III, whereas the non-linearity of the constitutive equation in phase II is due to increasing numbers of mobilized interfaces with increasing pressure gradient [29].

We show in Figure 9 the constitutive equations be-

tween volumetric flow rate and excess pressure drop $\Delta P - P_t$ for the dynamic pore network model for different saturations. The position of the spin glass transition in the spin model is marked in each plot. We see that apart from the smallest or the largest saturations we considered, there is coincidence between the transition Ib-II and the spin glass transition. We claim that they are same the same.

We note that phase II does not show hysteresis, see [64]. This is on the other hand a characteristics of phase Ib. There are also the strong fluctuations and long relaxation times associated with phase Ib [20, 21, 26]. We claim phase I to be a glassy phase.

One obvious next step beyond this paper is to use experimental data as input for the Boltzmann learning algorithm. However, we see a need for a better understanding of the spin model that the algorithm produces. We also observed that the choice of the learning rate η influences the coupling constant distribution strongly, even though each choice does reproduce the correlations in the flow model. What is the significance of this observation? What else can the spin model tell us about the physics of the flow model? Is there a meaning to the concept of temperature in the spin model and is it in any way connected to the concept of agitation (“agitation temperature”) in the flow model [35, 36]?

ACKNOWLEDGMENT

We thank Steffen Berg, Daan Frenkel and Sauro Succi for helpful discussions.

This work was partly supported by the Research Council of Norway through its Centers of Excellence funding scheme, project number 262644, and the INT-PART program, project number 309139. SS and AH furthermore acknowledge funding from the European Research Council (Grant Agreement 101141323 AGI-PORE). HC and JSA thank the Brazilian agencies CNPq, CAPES, FUNCAP and the National Institute of Science and Technology for Complex Systems (INCT-SC) for financial support.

-
- [1] J. Nittmann, G. Daccord, and H. E. Stanley, *Fractal growth viscous fingers: quantitative characterization of a fluid instability phenomenon*, *Nature* **314**, 141 (1985); DOI:10.1038/314141a0.
 - [2] B. B. Mandelbrot, *The Fractal Geometry of Nature* (W. H. Freeman. San Fransisco, 1977).
 - [3] J. Feder, *Fractals* (Plenum, New York, 1988).
 - [4] R. Lenormand, E. Touboul and C. Zarcone, *Numerical models and experiments on immiscible displacements in porous media*, *J. Fluid Mech.* **189**, 165 (1988); DOI:10.1017/S0022112088000953.
 - [5] J. Feder, E. G. Flekkøy and A. Hansen, *Physics of Flow in Porous Media* (Cambridge U. Press, Cambridge, 2022).
 - [6] A. L. Barabási and H. E. Stanley, *Fractal Concepts in Surface Growth*, (Cambridge University Press, Cambridge, 1995).
 - [7] S. Berg, R. T. Armstrong, M. Rücker, A. Hansen, S. Kjelstrup and D. Bedeaux, *From interface dynamics to Darcy scale description of multiphase flow in porous media*, 2026, *J. Coll. Interf. Sci.* **351**, 103791; DOI:10.1016/j.cis.2026.103791.
 - [8] D. G. Avraam and A. C. Payatakes, *Flow regimes and relative permeabilities during steady-state two-phase flow in porous media*, 2006, *J. of Fluid Mech.* **293**, 207; DOI:10.1017/S0022112095001698.
 - [9] K. T. Tallakstad, H. A. Knudsen, T. Ramstad, G. Løvoll, K. J. Måløy, R. Toussaint and E. G. Flekkøy, *Steady-state two-phase flow in porous media: Statistics and transport properties*, 2009, *Phys. Rev. Lett.* **102**, 074502; DOI:10.1103/PhysRevLett.102.074502.
 - [10] K. T. Tallakstad, G. Løvoll, H. A. Knudsen, T. Ram-

- stad, E. G. Flekkøy and K. J. Måløy, *Steady-state simultaneous two-phase flow in porous media: an experimental study*, 2009, *Phys. Rev. E*, **80**, 036308; DOI:10.1103/PhysRevE.80.036308.
- [11] E. M. Rassi, S. L. Codd and J. D. Seymour, *Nuclear magnetic resonance characterization of the stationary dynamics of partially saturated media during steady-state infiltration flow*, *New J. Phys.* **13**, 015007 (2011); DOI:10.1088/1367-2630/13/1/015007.
- [12] E. M. Rassi, S. L. Codd and J. D. Seymour, *Corrigendum: Nuclear magnetic resonance characterization of the stationary dynamics of partially saturated media during steady-state infiltration flow*, *New J. Phys.* **16**, 039501 (2014); DOI:10.1088/1367-2630/16/3/039501.
- [13] S. Sinha and A. Hansen, *Effective rheology of immiscible two-phase flow in porous media*, *EPL*, **99**, 44004 (2012); DOI:10.1209/0295-5075/99/44004.
- [14] A. G. Yiotis, L. Talon, and D. Salin, *Blob population dynamics during immiscible two-phase flows in reconstructed porous media*, *Phys. Rev. E*, **87**, 033001; DOI:10.1103/PhysRevE.87.033001.
- [15] O. Aursjø, M. Erpelding, K. T. Tallakstad, E. G. Flekkøy, A. Hansen and K. J. Måløy, *Film flow dominated simultaneous flow of two viscous incompressible fluids through a porous medium*, *Front. Phys.* **2**, 63 (2014); DOI:10.3389/fphy.2014.00063.
- [16] S. Sinha, A. T. Bender, M. Danczyk, K. Keepseagle, C. A. Prather, J. M. Bray, L. W. Thrane, J. D. Seymour, S. L. Codd and A. Hansen, *Effective rheology of two-phase flow in three-dimensional porous media: Experiment and simulation*, *Transp. Porous Med.* **119**, 77 (2017); DOI:10.1007/s11242-017-0874-4.
- [17] Y. Gao, Q. Lin, B. Bijeljic and M. J. Blunt, *X-ray microtomography of intermittency in multiphase flow at steady state using a differential imaging method*, *Water Res. Res.* **53**, 10274 (2017); DOI:10.1002/2017WR021736.
- [18] A. G. Yiotis, A. Dollari, M. E. Kainourgiakis, D. Salin and L. Talon, *Nonlinear Darcy flow dynamics during ganglia stranding and mobilization in heterogeneous porous domains*, *Phys. Rev. Fluids*, **4**, 114302 (2019); DOI:10.1103/PhysRevFluids.4.114302.
- [19] S. Roy, A. Hansen and S. Sinha, *Effective rheology of two-phase flow in a capillary fiber bundle model*, *Front. Phys.* **7**, 92 (2019); DOI:10.3389/fphy.2019.00092.
- [20] Y. Gao, Q. Lin, B. Bijeljic and M. J. Blunt, *Pore-scale dynamics and the multiphase Darcy law*, *Phys. Rev. Fluids*, **5**, 013801 (2020); DOI:10.1103/PhysRevFluids.5.013801.
- [21] Y. Zhang, B. Bijeljic, Y. Gao, Q. Lin and M. J. Blunt, *Quantification of non-linear multiphase flow in porous media*, *Geophys. Res. Lett.* **48**, e2020GL090477 (2021); DOI:10.1029/2020GL090477.
- [22] H. Fyhn, S. Sinha, S. Roy and A. Hansen, *Rheology of immiscible two-phase flow in mixed wet porous media: Dynamic pore network model and capillary fiber bundle model results*, *Trans. in Porous Med.* **139**, 491 (2021); DOI:10.1007/s11242-021-01674-3.
- [23] Y. Zhang, B. Bijeljic and M. J. Blunt, *Nonlinear multiphase flow in hydrophobic porous media*, *J. Fluid Mech.* **934**, R3 (2022); DOI:10.1017/jfm.2021.1148.
- [24] J. M. A. Sales, H. J. Seybold, C. L. N. Oliveira and J. S. Andrade Jr. *Bubble dynamics in stationary two-phase flow through disordered porous media*, *Front. Phys.* **10**, 860190 (2022); DOI:10.3389/fphy.2022.860190.
- [25] H. Fyhn, S. Sinha and A. Hansen, *Effective rheology of immiscible two-phase flow in porous media consisting of random mixtures of grains having two types of wetting properties*, *Front. Phys.* **11**, 1175426 (2023); DOI:10.3389/fphy.2023.1175426.
- [26] R. T. Armstrong, J. E. McClure, M. A. Berrill, M. Rücker, S. Schlüter and S. Berg, *Beyond Darcy's law: the role of phase topology and ganglion dynamics for two-fluid flow*, 2016, *Phys. Rev. E*, **94** 043113 (2016); DOI:10.1103/PhysRevE.94.043113.
- [27] J. E. McClure, S. Berg and R. T. Armstrong, *Capillary fluctuations and energy dynamics for flow in porous media*, *Phys. Fluids*, **33**, 083323 (2021); DOI:10.1063/5.0057428.
- [28] G. Foffi, E. Zaccarelli, F. Sciortino, P. Tartaglia and K. A. Dawson, *Kinetic Arrest Originating in Competition Between Attractive Interaction and Packing Force*, 2000, *J. Stat. Phys.* **100**, 363; DOI:10.1023/A:1018660200206.
- [29] S. Roy, S. Sinha and A. Hansen, *Effective rheology in the continuum limit*, 2024, *Transp. Porous Med.* **151**, 1295; DOI:10.1007/s11242-024-02073-0.
- [30] K. Binder and A. P. Young, *Spin glasses: Experimental facts, theoretical concepts, and open questions*, 1986, *Rev. Mod. Phys.* **58**, 801; DOI:10.1103/RevModPhys.58.801.
- [31] L. Meshulam and W. Bialek, *Statistical mechanics for networks of real neurons*, 2025, *Rev. Mod. Phys.* **97**, 045002; DOI:10.1103/jern-3nrc.
- [32] S. Sinha, M. Aa. Gjennestad, M. Vassvik and A. Hansen, *Fluid meniscus algorithms for dynamic pore network modeling of immiscible two-phase flow in porous media*, 2021, *Front. Phys.* **8**, 548497; DOI:10.3389/fphy.2020.548497.
- [33] E. T. Jaynes, *Information theory and statistical mechanics*, 1957, *Physical Review*, **106**, 620; DOI:10.1103/PhysRev.106.620.
- [34] E. T. Jaynes, *Information theory and statistical mechanics II*, 1957, *Physical Review*, **108**, 171; DOI:10.1103/PhysRev.108.171.
- [35] A. Hansen, E. G. Flekkøy, S. Sinha and P. A. Slotte, *A statistical mechanics framework for immiscible and incompressible two-phase flow in porous media*, 2023, *Adv. Water Res.* **171**, 104336; DOI:10.1016/j.advwatres.2022.104336.
- [36] A. Hansen and S. Sinha, *Thermodynamics-like formalism for immiscible and incompressible two-phase flow in porous media*, 2025, *Entropy*, **27**, 121; DOI:10.3390/e27020121.
- [37] N. K. Karadimitriou, S. M. Hassanizadeh, V. Joekar-Niasar and P. J. Kleingeld, *Micromodel study of two-phase flow under transient conditions: Quantifying effects of specific interfacial area*, *Water Resources Res.* **50**, 8125 (2014); DOI:10.1002/2014WR015388.
- [38] O. Aursjø, G. Løvoll and H. A. Knudsen, E. G. Flekkøy and K. J. Måløy, *A Direct Comparison Between a Slow Pore Scale Drainage Experiment and a 2D Lattice Boltzmann Simulation*, *Transp. Porous Med.* **86**, 125 (2011); DOI:10.1007/s11242-010-9611-y.
- [39] V. Joekar-Niasar and S. M. Hassanizadeh, *Analysis of fundamentals of two-phase flow in porous media using dynamic pore network models: A review*, *Crit. Rev. Environ. Sci. Technol.* **42**, 1895 (2012); DOI:10.1080/10643389.2011.574101.
- [40] M. Moura, D. Bedeaux, R. T. Armstrong and S.

- Kjelstrup, *Fluctuation–dissipation theorems in porous media two-phase flow: statistical characterisation of saturation fluctuations and measurement of Onsager coefficients*, *J. Fluid Mech.* **1026**, A2 (2026); DOI:10.1017/jfm.2025.10987.
- [41] S. F. Edwards and P. W. Anderson, *Theory of spin glasses*, *J. Phys. F: Metal Phys.* **5**, 965 (1975); DOI:10.1088/0305-4608/5/5/017.
- [42] D. Sherrington and S. Kirkpatrick, *Solvable model of a spin-glass*, *Phys. Rev. Lett.* **35**, 1792 (1975); DOI:10.1103/PhysRevLett.35.1792.
- [43] G. Parisi, *Nobel Lecture: Multiple equilibria*, arXiv:2304.00580v3 (2023); DOI:10.48550/arXiv.2304.00580.
- [44] E. W. Washburn, *The dynamics of capillary flow*, **17**, 273 (1921); DOI:10.1103/PhysRev.17.273.
- [45] F. A. L. Dullien, *Porous Media: Fluid, Transport and Pore Structure*, (Academic Press, San Diego, 1992).
- [46] S. Sinha, A. Hansen, D. Bedeaux and S. Kjelstrup, *Effective rheology of bubbles moving in a capillary tube*, *Phys. Rev. E* **87**, 025001 (2013); DOI:10.1103/PhysRevE.87.025001.
- [47] E. Aker, K. J. Måløy, A. Hansen and G. G. Batrouni, *A two-dimensional network simulator for two-phase flow in porous media*, *Transp. Porous Med.* **32**, 163 (1998); DOI:10.1023/A:1006510106194.
- [48] G. G. Batrouni and A. Hansen, *Fourier acceleration of iterative processes in disordered systems*, *J. Stat. Phys.* **52**, 747 (1988); DOI:10.1007/BF01019728.
- [49] S. Roy, H. Pedersen, S. Sinha and A. Hansen, *The co-moving velocity in immiscible two-phase flow in porous media*, 2022, *Transp. in Porous Media*, **143**, 69; DOI:10.1007/s11242-022-01783-7.
- [50] A. Hansen, S. Sinha, D. Bedeaux, S. Kjelstrup, M. Aa. Gjennestad and M. Vassvik, *Relations between seepage velocities in immiscible, incompressible two-phase flow in porous media*, *Transp. Porous Med.* **125**, 565 (2018); DOI:10.1007/s11242-018-1139-6.
- [51] S. Sinha, Y. Méheust, H. Fyhn, S. Roy and A. Hansen, *Disorder-induced non-linear growth of fingers in immiscible two-phase flow in porous media*, *Phys. Fluids* **36**, 033309 (2024); DOI:10.1063/5.0193570.
- [52] T. Ezaki, E. F. dos Reis and N. Masuda, *Closer to critical resting-state neural dynamics in individuals with higher fluid intelligence*, *Comm. Bio.* **3**, 52 (2020); DOI:10.1038/s42003-020-0774-y.
- [53] C. I. N. S. Filho, L. de Arcangelis, H. J. Herrmann, D. Plenz, P. Kells, T. L. Ribeiro and J. S. Andrade Jr., *Ising-like model replicating time-averaged spiking behaviour of in vitro neuronal networks*, *Sci. Rep.* **14**, 7002 (2024); DOI:10.1038/s41598-024-55922-9.
- [54] C. I. N. S. Filho, R. S. Pires, H. A. Carmona, J. S. Andrade Jr, *Mapping inter-city trade networks to maximum entropy models using electronic invoice data*, *Chaos, Solitons and Fractals* **202**, 117593 (2026); DOI:10.1016/j.chaos.2025.117593.
- [55] W. Bialek, A. Cavagna, I. Giardina, T. Mora, E. Silvestri, M. Viale and A. M. Walczak, *Statistical mechanics for natural flocks of birds*, *Proc. Natl. Acad. Sci. USA* **109**, 4786 (2012); DOI:10.1073/pnas.1118633109.
- [56] W. Bialek, A. Cavagna, I. Giardina, T. Mora, O. Pohl, E. Silvestri, M. Viale and A. M. Walczak, *Social interactions dominate speed control in poising natural flocks near criticality*, *Proc. Natl. Acad. Sci. USA* **111**, 7212 (2014); DOI:10.1073/pnas.1324045111.
- [57] K. Binder and D. Landau, *A Guide to Monte Carlo Simulations in Statistical Physics* (Cambridge University Press, Cambridge, 2025).
- [58] L. Prechelt, in *Neural Networks: Tricks of the Trade*, edited by G. Montavon, G. B. Orr and K. R. Müller (Springer, Berlin, 2012); DOI:10.1007/978-3-642-35289-8_5.
- [59] K. H. Fischer and J. A. Hertz, *Spin glasses* (Cambridge University Press, Cambridge, 1991).
- [60] S. Roux and H. J. Herrmann, *Disorder-induced non-linear conductivity*, *Europhys. Lett.* **1227**, 4 (1987); DOI:10.1209/0295-5075/4/11/003.
- [61] L. Talon and A. Hansen, *Effective rheology of bi-viscous non-Newtonian fluids in porous media*, *Front. Phys.* **7**, 225 (2020); DOI:10.3389/fphy.2019.00225.
- [62] C. Spurin, T. Bultreys, B. Bijeljic, M. J. Blunt and S. Krevor, *Intermittent fluid connectivity during two-phase flow in a heterogeneous carbonate rock*, *Phys. Rev. E* **100**, 043103 (2019); DOI:10.1103/PhysRevE.100.043103.
- [63] A. G. Yiotis, A. Dollari, M. E. Kainourgiakis, D. Salin and L. Talon, *Nonlinear Darcy flow dynamics during ganglia stranding and mobilization in heterogeneous porous domains*, *Phys. Rev. Fluids* **4**, 114302 (2019); DOI:10.1103/PhysRevFluids.4.114302.
- [64] M. Erpelding, S. Sinha, K. T. Tallakstad, A. Hansen, E. G. Flekkøy and K. J. Måløy, *History independence of steady state in simultaneous two-phase flow through two-dimensional porous media*, *Phys. Rev. E* **88**, 053004 (2013); DOI:10.1103/PhysRevE.88.053004.